Kukkola, Jarno; Hinkkanen, Marko

State Observer for Grid-Voltage Sensorless Control of a Converter Equipped with an LCL Filter: Direct Discrete-Time Design

Published in:
IEEE Transactions on Industry Applications

DOI:
10.1109/TIA.2016.2542060

Published: 01/07/2016

Document Version
Peer reviewed version

Please cite the original version:
Kukkola, J., & Hinkkanen, M. (2016). State Observer for Grid-Voltage Sensorless Control of a Converter Equipped with an LCL Filter: Direct Discrete-Time Design. *IEEE Transactions on Industry Applications*, *52*(4), 3133-3145. [7433435]. https://doi.org/10.1109/TIA.2016.2542060

State Observer for Grid-Voltage Sensorless Control of a Converter Equipped With an LCL Filter: Direct Discrete-Time Design

Jarno Kukkola and Marko Hinkkanen, *Senior Member, IEEE*

***Abstract*—Synchronization with the power system is an essential part of control of grid-connected converters. This paper proposes a grid-voltage sensorless synchronization and control scheme for a converter equipped with an LCL filter, measuring only the converter currents and the DC voltage. A discrete-time pole-placement design method is used to formulate an adaptive full-order observer for estimation of the frequency, angle, and magnitude of the grid voltage. The proposed discrete-time design method enables straightforward implementation and suits low sampling rates better than its continuous-time counterpart. The analytically derived design is experimentally validated, and the results demonstrate rapid convergence of the estimated quantities. Moreover, the experimental tests show that grid-voltage sensorless operation is possible under balanced and unbalanced grid disturbances and distorted grid conditions.**

***Index Terms*—Active front-end rectifier, adaptive observer, distributed generation, line-voltage sensorless, small-signal linearization, state feedback, synchronization.**

I. Introduction

Grid-connected converters are increasingly used to connect various renewable energy sources to the electric power system. A growing trend is to replace a conventional inductive L filter (between the converter and the grid) with an LCL filter in order to fulfill the current harmonic limits presented in the standards, e.g., [1]. A factor behind this trend is higher switching harmonics attenuation provided by the LCL filter, which enables a physically smaller and cheaper filter at low switching frequencies, e.g., $4 \ldots 8$ kHz [2].

The converter equipped with an LCL filter is also an attractive solution for low-harmonic active front-end rectifiers of variable-speed motor drives, where regenerative braking, adjustable DC-link voltage, and adjustable power factor enable energy flow optimization. In drives, operation without position or speed sensors provides cost savings and increases reliability [3]. Overall costs of a drive with an active front-end rectifier can be further reduced by replacing the grid-voltage sensors with estimation and implementing active damping of the LCL-filter resonance without extra sensors as, e.g., in [4].

At high power ratings, the sensor-cost savings are less significant or even meaningless, since the overall system costs are high. However, an option for grid-voltage sensorless operation can provide redundancy, e.g., in the case of sensor (including wiring and measuring interfaces) failures. Alternatively, in some applications, the available grid-voltage estimate may enable use of low-cost sensors. This kind of application could be, e.g., a solar inverter. At least, their investment costs are predicted to fall significantly (even to a fifth of today's prices by 2050) [5].

Synchronization with the grid is needed in order to control instantaneous active and reactive power injected by the converter. However, only a few grid-voltage sensorless synchronization and control methods have been presented in the case of the LCL filter [4], [6]–[12]. Sensorless synchronization has been obtained using the instantaneous power theory [4] and virtual flux models [6], [7]. Alternatively, the grid voltage can be estimated using observers [8]–[14]. Solutions relying on the Kalman filter have been proposed [8]–[10]. Although the Kalman filter can be described as a statistically optimal estimator, its drawback is that the process noise parameters are needed for tuning of the observer. These noise parameters are often determined by trial and error [8]. If a grid-voltage sensorless synchronization and control system is carefully designed, it can operate even under unbalanced and distorted grid conditions [6], [7], [9], [15], [16].

A subcategory of the observers consists of model-reference adaptive observers, which are able to adjust internal model parameters in real time. Adaptive observers have been used for estimation of the rotor speed, position, and flux magnitude in motor drives, e.g., in [17], and, correspondingly, for estimation of the grid-voltage frequency, angle, and magnitude in grid-connected converters [9], [11]–[14]. The estimation error of the converter current includes the information of the grid-voltage angle and amplitude [12], [13].

Control of a converter is typically implemented on a microprocessor and the sampling of the converter current is synchronized with the pulse-width modulation (PWM). Frequently, the control algorithms are designed in the continuous-time domain and then discretized. This principle works well in many cases. However, when the LCL-filter resonance is relatively close to the switching frequency, only a few samples are obtained within the period of the resonance frequency. Then, the direct discrete-time design is preferable, e.g., in the case of current control [18]. For sensorless control of a converter equipped with an LCL filter, a continuous-time design has been presented for an adaptive full-order observer in [12]. However, no analytical direct discrete-time design method has been presented for the adaptive full-order observer in this application.

This work deals with grid-voltage sensorless control of a

J. Kukkola and M. Hinkkanen are with Aalto University, Department of Electrical Engineering and Automation, Espoo, Finland (e-mail: jarno.kukkola@aalto.fi; marko.hinkkanen@aalto.fi).

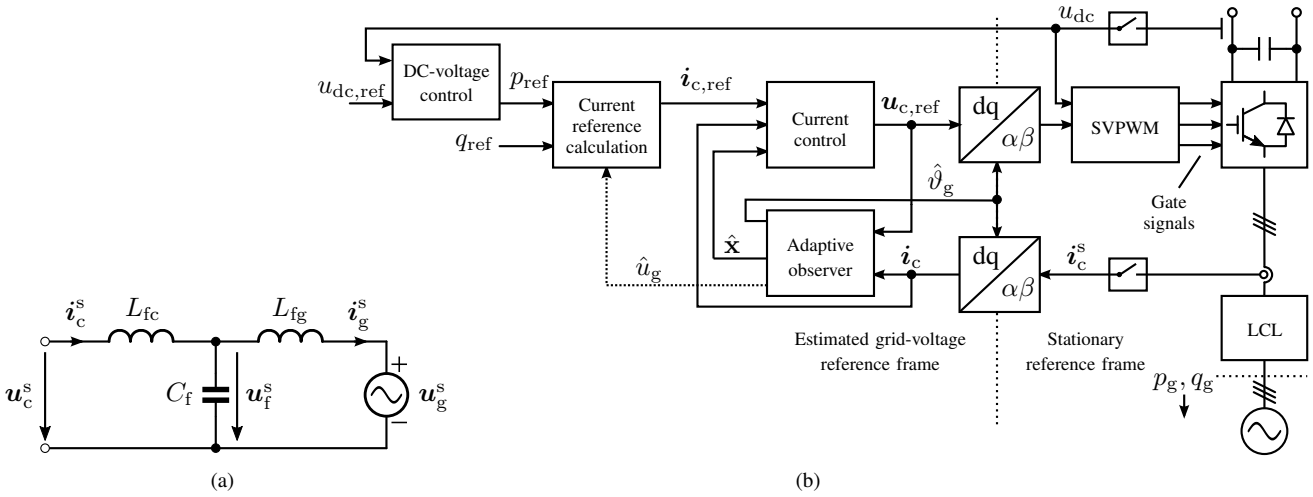

Fig. 1. (a) Space-vector circuit model of the grid-connected LCL filter in stationary coordinates (marked with the superscript s). (b) Grid-voltage sensorless control system. The angle $\omega_{\mathrm{g}} T_{\mathrm{s}}$ caused by the computational delay is compensated for in the dq $\rightarrow \alpha\beta$ transformation (not explicitly shown in the figure).

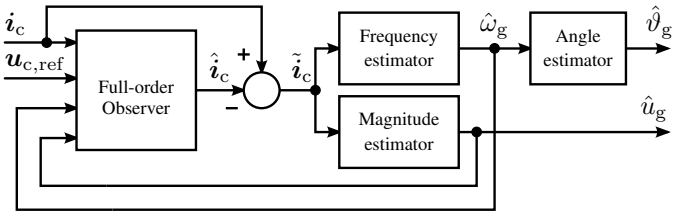

Fig. 2. Internal structure of the adaptive observer.

converter equipped with an LCL filter [19]. Main contributions of this paper are: 1) A direct discrete-time design method is proposed for an adaptive full-order observer enabling grid-voltage sensorless control; 2) Estimation-error dynamics of the observer are analyzed by means of small-signal linearization; 3) The proposed observer is experimentally tested as a part of a grid-voltage sensorless control system under balanced and unbalanced grid disturbances. Furthermore, the proposed observer is compared with the observer designed in the continuous-time domain [12]. The presented design method retains analytical connection between the physical model parameters of the LCL filter and the observer dynamics. This connection generalizes the method for different parameter sets and enables automatic tuning if the model parameters are known or estimated.

II. System Model

Switching-cycle-averaged complex-valued space vectors are used. Complex-valued, matrix, and vector quantities are marked with boldface symbols. The equivalent circuit model of the LCL filter is presented in Fig. 1(a). The grid-voltage vector in the stationary reference frame (marked with the superscript s) is

$$\boldsymbol{u}_{\mathrm{g}}^{\mathrm{s}} = \mathrm{e}^{\mathrm{j}\vartheta_{\mathrm{g}}} u_{\mathrm{g}} = u_{\mathrm{g}\alpha} + \mathrm{j} u_{\mathrm{g}\beta} \tag{1}$$

where $\vartheta_{\mathrm{g}} = \int \omega_{\mathrm{g}} \mathrm{d}t$ is the angle, ω_{g} is the angular frequency, and u_{g} is the amplitude. Furthermore, $u_{\mathrm{g}\alpha}$ and $u_{\mathrm{g}\beta}$ are the space-vector components.

In synchronous grid-voltage oriented coordinates (marked with the superscript g), the dynamics of the converter current $\boldsymbol{i}_{\mathrm{c}}^{\mathrm{g}}$ are

$$\begin{aligned} \frac{\mathrm{d}\mathbf{x}^{\mathrm{g}}}{\mathrm{d}t} &= \begin{bmatrix} -\mathrm{j}\omega_{\mathrm{g}} & -\frac{1}{L_{\mathrm{fc}}} & 0 \\ \frac{1}{C_{\mathrm{f}}} & -\mathrm{j}\omega_{\mathrm{g}} & -\frac{1}{C_{\mathrm{f}}} \\ 0 & \frac{1}{L_{\mathrm{fg}}} & -\mathrm{j}\omega_{\mathrm{g}} \end{bmatrix} \mathbf{x}^{\mathrm{g}} + \begin{bmatrix} \frac{1}{L_{\mathrm{fc}}} \\ 0 \\ 0 \end{bmatrix} \boldsymbol{u}_{\mathrm{c}}^{\mathrm{g}} - \begin{bmatrix} 0 \\ 0 \\ \frac{1}{L_{\mathrm{fg}}} \end{bmatrix} u_{\mathrm{g}} \\ \boldsymbol{i}_{\mathrm{c}}^{\mathrm{g}} &= \underbrace{\begin{bmatrix} 1 & 0 & 0 \end{bmatrix}}_{\mathbf{C}_{\mathrm{c}}} \mathbf{x}^{\mathrm{g}} \end{aligned} \tag{2}$$

where the state vector is $\mathbf{x}^{\mathrm{g}} = [\boldsymbol{i}_{\mathrm{c}}^{\mathrm{g}}, \boldsymbol{u}_{\mathrm{f}}^{\mathrm{g}}, \boldsymbol{i}_{\mathrm{g}}^{\mathrm{g}}]^{\mathrm{T}}$, the voltage across the filter capacitor C_{f} is $\boldsymbol{u}_{\mathrm{f}}^{\mathrm{g}}$, and the converter and grid currents are $\boldsymbol{i}_{\mathrm{c}}^{\mathrm{g}}$ and $\boldsymbol{i}_{\mathrm{g}}^{\mathrm{g}}$, respectively. The resonance frequency of the LCL filter is

$$\omega_{\mathrm{p}} = \sqrt{\frac{L_{\mathrm{fc}} + L_{\mathrm{fg}}}{L_{\mathrm{fc}} L_{\mathrm{fg}} C_{\mathrm{f}}}} \tag{3}$$

The losses of the filter (e.g., the series resistances of the inductors) are neglected, which represents the worst-case situation for the resonance of the LCL filter. The resonance is actively damped by a current controller, e.g., [18]. Therefore, additional damping resistors are not needed and, hence, not included in the model.

A zero-order hold for the switching-cycle-averaged converter output voltage is assumed and synchronous sampling is used. In addition, the amplitude u_{g} and frequency ω_{g} of the grid voltage are assumed to vary slowly, i.e., to be constant during the sampling period T_{s}. Under these assumptions, the discrete-time model of (2) is [18]

$$\begin{aligned} \mathbf{x}^{\mathrm{g}}(k+1) &= \boldsymbol{\Phi} \mathbf{x}^{\mathrm{g}}(k) + \boldsymbol{\Gamma}_{\mathrm{c}} \boldsymbol{u}_{\mathrm{c}}^{\mathrm{g}}(k) + \boldsymbol{\Gamma}_{\mathrm{g}} u_{\mathrm{g}}(k) \\ \boldsymbol{i}_{\mathrm{c}}^{\mathrm{g}}(k) &= \mathbf{C}_{\mathrm{c}} \mathbf{x}^{\mathrm{g}}(k) \end{aligned} \tag{4}$$

The closed-form expressions for the elements of the state-transition matrix $\boldsymbol{\Phi}$ and the input vectors $\boldsymbol{\Gamma}_{\mathrm{c}}$ and $\boldsymbol{\Gamma}_{\mathrm{g}}$ are given in Appendix A as functions of the LCL-filter parameters. The grid-voltage angle is

$$\vartheta_{\mathrm{g}}(k+1) = \vartheta_{\mathrm{g}}(k) + T_{\mathrm{s}} \omega_{\mathrm{g}} \tag{5}$$

in the discrete-time domain.

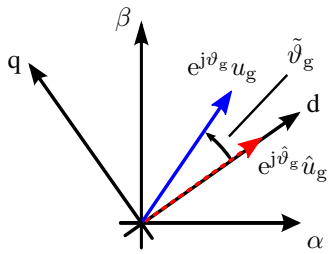

Fig. 3. Orientation of the estimated grid-voltage reference frame.

III. Adaptive Full-Order Observer

The control structure is illustrated in Fig. 1(b). Control of the converter is implemented in the estimated grid-voltage reference frame that is aligned with the estimated grid-voltage vector. Synchronization is obtained using an adaptive observer. The structure of the adaptive observer is shown in Fig. 2. The angular frequency $\hat{\omega}_g$, the angle $\hat{\vartheta}_g$, and the magnitude $\hat{u}_g$ of the grid voltage are estimated in the outer loops, while the state vector $\hat{\mathbf{x}}$ is estimated by the full-order state observer. The full-order observer is

$$\begin{aligned}\hat{\mathbf{x}}(k+1) &= \hat{\mathbf{\Phi}}\hat{\mathbf{x}}(k) + \hat{\mathbf{\Gamma}}_c\boldsymbol{u}_c(k) + \hat{\mathbf{\Gamma}}_g\hat{u}_g(k) \\ &\quad + \mathbf{K}_o[\boldsymbol{i}_c(k) - \hat{\boldsymbol{i}}_c(k)] \\ \hat{\boldsymbol{i}}_c(k) &= \mathbf{C}_c\hat{\mathbf{x}}(k)\end{aligned} \tag{6}$$

where $\boldsymbol{u}_c(k) = \boldsymbol{u}_{c,ref}(k-1)$ is obtained from the delayed converter-voltage reference, $\mathbf{K}_o = [\boldsymbol{k}_{o1}\ \boldsymbol{k}_{o2}\ \boldsymbol{k}_{o3}]^T$ is the observer gain vector, and $\hat{\mathbf{\Phi}}$, $\hat{\mathbf{\Gamma}}_c$, and $\hat{\mathbf{\Gamma}}_g$ are adaptive model matrices that are obtained replacing the actual angular frequency ω_g with the estimated angular frequency $\hat{\omega}_g$ in the matrices. According to (5), a natural estimator for the angle is

$$\hat{\vartheta}_g(k+1) = \hat{\vartheta}_g(k) + T_s\hat{\omega}_g(k) \tag{7}$$

A. Estimation-Error Dynamics

There can be an angle displacement $\tilde{\vartheta}_g = \vartheta_g - \hat{\vartheta}_g$ between the actual and estimated grid-voltage vector (cf. Fig. 3). From (5) and (7), the dynamics of the angle error become

$$\tilde{\vartheta}_g(k+1) = \tilde{\vartheta}_g(k) + T_s\tilde{\omega}_g(k) \tag{8}$$

where $\tilde{\omega}_g = \omega_g - \hat{\omega}_g$ is the frequency estimation error. Since the system model and the control algorithm are in the different coordinates, the discrete-time model (4) is transformed into the estimated grid-voltage reference frame applying:

$$\begin{aligned}\mathbf{x}^g(k+1) &= e^{-j\tilde{\vartheta}_g(k+1)}\mathbf{x}(k+1) \\ \mathbf{x}^g(k) &= e^{-j\tilde{\vartheta}_g(k)}\mathbf{x}(k) \\ \boldsymbol{u}_c^g(k) &= e^{-j\tilde{\vartheta}_g(k)}\boldsymbol{u}_c(k)\end{aligned} \tag{9}$$

Together with (8), the resulting dynamics are

$$\begin{aligned}\mathbf{x}(k+1) &= e^{jT_s\tilde{\omega}_g(k)}\mathbf{\Phi}\mathbf{x}(k) + e^{jT_s\tilde{\omega}_g(k)}\mathbf{\Gamma}_c\boldsymbol{u}_c(k) \\ &\quad + e^{j\tilde{\vartheta}_g(k+1)}\mathbf{\Gamma}_g u_g(k) \\ \boldsymbol{i}_c(k) &= \mathbf{C}_c\mathbf{x}(k)\end{aligned} \tag{10}$$

From (6), (8), and (10), the dynamics of the estimation error $\tilde{\mathbf{x}}(k) = \mathbf{x}(k) - \hat{\mathbf{x}}(k)$ become

$$\begin{aligned}\tilde{\mathbf{x}}(k+1) &= (\hat{\mathbf{\Phi}} - \mathbf{K}_o\mathbf{C}_c)\tilde{\mathbf{x}}(k) + \left(e^{jT_s\tilde{\omega}_g(k)}\mathbf{\Phi} - \hat{\mathbf{\Phi}}\right)\mathbf{x}(k) \\ &\quad + \hat{\mathbf{\Gamma}}_g\tilde{u}_g(k) + \left(e^{jT_s\tilde{\omega}_g(k)}\mathbf{\Gamma}_c - \hat{\mathbf{\Gamma}}_c\right)\boldsymbol{u}_c(k) \\ &\quad + \left(e^{j[\tilde{\vartheta}_g(k)+T_s\tilde{\omega}_g(k)]}\mathbf{\Gamma}_g - \hat{\mathbf{\Gamma}}_g\right)u_g(k)\end{aligned} \tag{11}$$

where $\tilde{u}_g = u_g - \hat{u}_g$ is the estimation error of the grid voltage.

As can be seen, (11) is nonlinear with respect to the angle error $\tilde{\vartheta}_g$ and the angular-frequency error $\tilde{\omega}_g$. Furthermore, the matrices $\hat{\mathbf{\Phi}}(\hat{\omega}_g)$, $\hat{\mathbf{\Gamma}}_c(\hat{\omega}_g)$, and $\hat{\mathbf{\Gamma}}_g(\hat{\omega}_g)$ are functions of the estimated angular frequency $\hat{\omega}_g$, and, therefore, depend on the estimation error $\tilde{\omega}_g$, since $\hat{\omega}_g = \omega_g - \tilde{\omega}_g$.

B. Small-Signal Linearization

The nonlinear dynamics are analyzed in an operating point. Operating-point quantities are marked with the subscript 0. If the accurate model parameters are assumed and the gain $\mathbf{K}_o$ is selected such that the eigenvalues of $\mathbf{\Phi} - \mathbf{K}_o\mathbf{C}_c$ are inside the unit circle, the system has an equilibrium point $\{\tilde{\mathbf{x}}_0 = 0,\ \tilde{u}_{g0} = 0,\ \tilde{\omega}_{g0} = 0,\ \tilde{\vartheta}_{g0} = 0\}$, where the estimation error is zero in steady state. In the vicinity of the equilibrium point, the system (11) has linearized dynamics

$$\begin{aligned}\tilde{\mathbf{x}}(k+1) &= (\mathbf{\Phi} - \mathbf{K}_o\mathbf{C}_c)\,\tilde{\mathbf{x}}(k) + j\mathbf{\Gamma}_g u_{g0}\tilde{\vartheta}_g(k) \\ &\quad + \underbrace{\left[j\mathbf{\Gamma}_g T_s - \left(\frac{d\hat{\mathbf{\Gamma}}_g}{d\tilde{\omega}_g}\right)_0\right]u_{g0}}_{\mathbf{\Gamma}_\omega}\tilde{\omega}_g(k) + \mathbf{\Gamma}_g\tilde{u}_g(k).\end{aligned} \tag{12}$$

The linearized dynamics are derived in Appendix B.

The converter current is the only measured state variable. Thus, it is interesting to analyze the dynamics of the estimation error $\tilde{\boldsymbol{i}}_c = \mathbf{C}_c\tilde{\mathbf{x}}$ of the converter current induced by the magnitude and angle deviations, $\tilde{u}_g$ and $\tilde{\vartheta}_g$, respectively. From (12), the pulse-transfer function from the grid-voltage estimation error to the converter-current estimation error is

$$\boldsymbol{G}_{iu}(z) = \frac{\tilde{\boldsymbol{i}}_c(z)}{\tilde{u}_g(z)} = \frac{\boldsymbol{b}(z)}{\boldsymbol{a}(z)} = \mathbf{C}_c(z\mathbf{I} - \mathbf{\Phi} + \mathbf{K}_o\mathbf{C}_c)^{-1}\mathbf{\Gamma}_g \tag{13}$$

where

$$\boldsymbol{a}(z) = \det(z\mathbf{I} - \mathbf{\Phi} + \mathbf{K}_o\mathbf{C}_c) \tag{14}$$

and $\boldsymbol{b}(z)$ is the numerator of the transfer function. The coefficient $\mathbf{\Gamma}_\omega$ in (12) is minor in comparison with the other coefficients and

$$\lim_{T_s\to 0}\mathbf{\Gamma}_\omega = 0 \tag{15}$$

Therefore, the dynamics can be simplified by approximating $\mathbf{\Gamma}_\omega \approx 0$, and the pulse-transfer function from the angle error to the converter current estimation error becomes

$$\boldsymbol{G}_{i\vartheta}(z) = \frac{\tilde{\boldsymbol{i}}_c(z)}{\tilde{\vartheta}_g(z)} = \frac{ju_{g0}\cdot\boldsymbol{b}(z)}{\boldsymbol{a}(z)} \tag{16}$$

It can be seen that the estimation-error components in $\tilde{\boldsymbol{i}}_c$ caused by the voltage and angle errors are orthogonal, i.e., $\boldsymbol{G}_{i\vartheta} = ju_{g0}\boldsymbol{G}_{iu}$. This forms the basis for the design of the adaptation loops in Sections III-D and III-E.

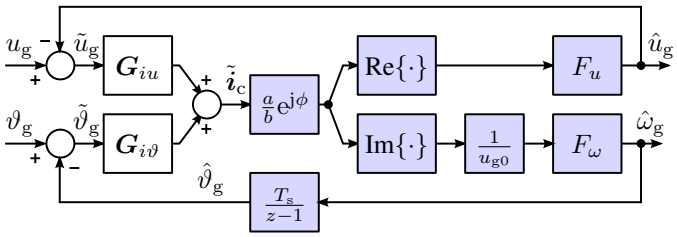

Fig. 4. Small-signal linearized adaptation loops. The blue blocks represent the adaptation laws, i.e., the estimators. For simplicity, the current error component caused by the angular-frequency error $\tilde{\omega}_\mathrm{g}$ is omitted in the figure, since its coefficient is minor in (12).

C. Pole Placement of the Full-Order Observer

Let the desired characteristic polynomial (14) of the estimation-error dynamics be

$$\boldsymbol{a}(z) = (z-\alpha_{\mathrm{o}1})(z-\boldsymbol{\alpha}_{\mathrm{o}2})(z-\boldsymbol{\alpha}_{\mathrm{o}3}). \tag{17}$$

The discrete-time poles $\alpha_{\mathrm{o}1}$, $\boldsymbol{\alpha}_{\mathrm{o}2}$, and $\boldsymbol{\alpha}_{\mathrm{o}3}$ are mapped via the continuous-time counterpart $(s+\alpha_{\mathrm{od}})(s^2+2\zeta_{\mathrm{or}}\omega_{\mathrm{or}}s+\omega_{\mathrm{or}}^2)$:

$$\begin{aligned}\alpha_{\mathrm{o}1} &= \exp\left(-\alpha_{\mathrm{od}}T_\mathrm{s}\right)\\ \boldsymbol{\alpha}_{\mathrm{o}2,3} &= \exp[(-\zeta_{\mathrm{or}} \pm \mathrm{j}\sqrt{1-\zeta_{\mathrm{or}}^2})\omega_{\mathrm{or}}T_\mathrm{s}]\end{aligned} \tag{18}$$

Continuous-time pole locations are the tuning parameters of the full-order observer. The first-order pole α_{od} is set to determine the dominant dynamics of the estimation error. The pair of poles, determined by ω_{or} and ζ_{or}, is placed at a higher frequency. Analytical expressions for calculating the observer gain $\mathbf{K}_\mathrm{o}$ have been derived in [18] as a function of the tuning and system (LCL filter) parameters. Furthermore, the selection of the pole locations has been explained in [18].

D. Quasi-Steady-State Analysis

In order to design adaptation laws for the angle and amplitude estimation of the grid voltage, the estimation error dynamics of the full-order observer in (12) are considered to be much faster than the adaptation mechanisms. From adaptation point of view, it is reasonable to approximate the full-order observer dynamics using quasi-steady-state gains. These gains are obtained for $\tilde{u}_\mathrm{g}$ and $\tilde{\vartheta}_\mathrm{g}$ in (13) and (16), respectively, by making $z=1$. It follows that

$$\tilde{\boldsymbol{i}}_\mathrm{c} = \underbrace{\mathrm{e}^{-\mathrm{j}\phi}(b/a)}_{\boldsymbol{G}_{iu}(1)}\tilde{u}_\mathrm{g} + \underbrace{\mathrm{j}u_{\mathrm{g}0}\mathrm{e}^{-\mathrm{j}\phi}(b/a)}_{\boldsymbol{G}_{i\vartheta}(1)}\tilde{\vartheta}_\mathrm{g} \tag{19}$$

where the constants are

$$\begin{aligned}\phi &= (3/2)\omega_\mathrm{g}T_\mathrm{s}\\ a &= \omega_\mathrm{g}C_\mathrm{f}L_{\mathrm{fc}}L_{\mathrm{fg}}(\omega_\mathrm{g}^2-\omega_\mathrm{p}^2)(1-\alpha_{\mathrm{o}1})(1-\boldsymbol{\alpha}_{\mathrm{o}2})(1-\boldsymbol{\alpha}_{\mathrm{o}3})\\ b &= 4\sin(\omega_\mathrm{g}T_\mathrm{s}/2)[\cos(\omega_\mathrm{g}T_\mathrm{s})-\cos(\omega_\mathrm{p}T_\mathrm{s})]\end{aligned} \tag{20}$$

and ω_p is the resonance frequency (3).

As revealed in (19), the real part of the estimation error $\tilde{\boldsymbol{i}}_\mathrm{c}$ of the converter current is strongly affected by the voltage difference $\tilde{u}_\mathrm{g}$. On the other hand, the imaginary part of $\tilde{\boldsymbol{i}}_\mathrm{c}$ is strongly affected by the angle difference $\tilde{\vartheta}_\mathrm{g}$. Moreover, if the current-estimation error $\tilde{\boldsymbol{i}}_\mathrm{c}$ is rotated and scaled as $\tilde{\boldsymbol{i}}_\mathrm{c}' = (a/b)\mathrm{e}^{\mathrm{j}\phi}\tilde{\boldsymbol{i}}_\mathrm{c}$, the real and imaginary parts of the modified error $\tilde{\boldsymbol{i}}_\mathrm{c}'$ can be directly separated into the grid-voltage magnitude and angle estimation, respectively.

E. Adaptation Laws

Let the grid-voltage estimator be

$$\hat{u}_\mathrm{g}(z) = \underbrace{\frac{k_{\mathrm{i,u}}}{z-1}}_{F_u(z)}\mathrm{Re}\left\{\frac{a}{b}\mathrm{e}^{\mathrm{j}\phi}\tilde{\boldsymbol{i}}_\mathrm{c}(z)\right\} \tag{21}$$

where $k_{\mathrm{i,u}}$ is the gain, and the estimator for the angular frequency be

$$\hat{\omega}_\mathrm{g}(z) = \frac{1}{u_{\mathrm{g}0}}\underbrace{\left(k_{\mathrm{p},\omega}+\frac{k_{\mathrm{i},\omega}}{z-1}\right)}_{F_\omega(z)}\mathrm{Im}\left\{\frac{a}{b}\mathrm{e}^{\mathrm{j}\phi}\tilde{\boldsymbol{i}}_\mathrm{c}(z)\right\} \tag{22}$$

where $k_{\mathrm{p},\omega}$ and $k_{\mathrm{i},\omega}$ are the gains. Furthermore, the estimator for the grid-voltage angle is given in (7). The angular frequency estimator directly amplifies the current-estimation error $\tilde{\boldsymbol{i}}_\mathrm{c}$ through the proportional part of $F_\omega(z)$, thus some noise in $\hat{\omega}_\mathrm{g}$ might be present in a practical implementation. A naturally filtered estimate for the frequency is obtained from the integral of (22), and it is

$$\hat{\omega}_{\mathrm{gf}}(z) = \frac{1}{u_{\mathrm{g}0}}\underbrace{\frac{k_{\mathrm{i},\omega}}{z-1}}_{F_{\omega\mathrm{f}}(z)}\mathrm{Im}\left\{\frac{a}{b}\mathrm{e}^{\mathrm{j}\phi}\tilde{\boldsymbol{i}}_\mathrm{c}(z)\right\} \tag{23}$$

While the estimate $\hat{\omega}_\mathrm{g}$ is internally used in the observer, the estimate $\hat{\omega}_{\mathrm{gf}}$ with reduced noise is useful, e.g., for monitoring purposes and for other control loops of the converter.

Fig. 4 shows the linearized adaptation loops, when the proposed adaptation laws are used. Considering the quasi-steady-state relationships $\boldsymbol{G}_{iu}(1)$ and $\boldsymbol{G}_{i\vartheta}(1)$ according to (19), two separate feedback loops are obtained. The closed-loop transfer function of the linearized grid-voltage magnitude adaptation loop becomes

$$G_u(z) = \frac{\hat{u}_\mathrm{g}(z)}{u_\mathrm{g}(z)} = \frac{F_u(z)}{1+F_u(z)} = \frac{k_{\mathrm{i,u}}}{z+k_{\mathrm{i,u}}-1} \tag{24}$$

If the gain is

$$k_{\mathrm{i,u}} = 1-\exp(-\alpha_\mathrm{u}T_\mathrm{s}) \tag{25}$$

the closed-loop transfer function $G_u(z)$ represents the first-order system with the bandwidth of α_u. This bandwidth is the only parameter needed for tuning of the grid-voltage-magnitude estimation loop. Fig. 5(a) illustrates the estimation error of the voltage when a step change Δu_g is applied in u_g and the parameters are $\alpha_\mathrm{u} = 2\pi\cdot 50$ rad/s and $\alpha_\mathrm{u} = 2\pi\cdot 100$ rad/s. The estimation error is less than 5% after $t_{5\%}\approx 3/\alpha_\mathrm{u}$. Moreover, the error is practically zero even for the lower α_u after one 20-ms period of the grid voltage.

The closed-loop transfer function of the linearized angle adaptation loop becomes

$$\begin{aligned}G_\vartheta(z) = \frac{\hat{\vartheta}_\mathrm{g}(z)}{\vartheta_\mathrm{g}(z)} &= \frac{F_\omega(z)\frac{T_\mathrm{s}}{z-1}}{1+F_\omega(z)\frac{T_\mathrm{s}}{z-1}}\\ &= \frac{T_\mathrm{s}(k_{\mathrm{p},\omega}z+k_{\mathrm{i},\omega}-k_{\mathrm{p},\omega})}{z^2+(k_{\mathrm{p},\omega}T_\mathrm{s}-2)z+k_{\mathrm{i},\omega}T_\mathrm{s}-k_{\mathrm{p},\omega}T_\mathrm{s}+1}\end{aligned} \tag{26}$$

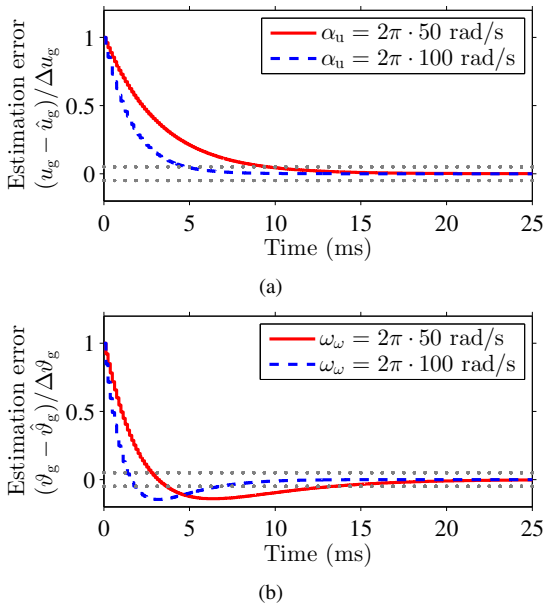

Fig. 5. Estimation-error responses: (a) step change Δu_g is applied in the grid-voltage magnitude u_g at $t = 0$ in (24); (b) step change $\Delta\vartheta_g$ is applied in the angle ϑ_g at $t = 0$ in (26). The tuning parameters of the adaptation loops are varied according to the legends. The damping ratio is $\zeta_\omega = 1$. The 5-% settling limits are marked with dotted lines.

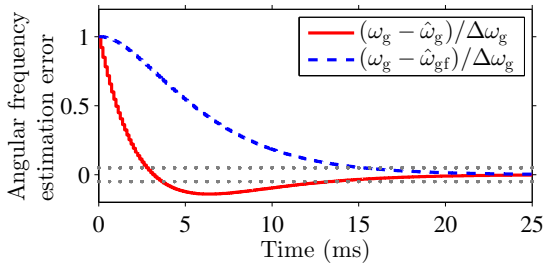

Fig. 6. Estimation-error responses when a step change $\Delta\omega_g$ is applied in ω_g: (solid line) angular-frequency estimate $\hat{\omega}_g$; (dashed line) angular-frequency estimate $\hat{\omega}_{gf}$. The tuning parameters of the adaptation loop are: $\omega_\omega = 2\pi \cdot 50$ rad/s and $\zeta_\omega = 1$. The 5-% settling limits are marked with dotted lines.

Selecting the gains

$$\begin{aligned} k_{p,\omega} &= [2 - 2 \cdot \exp(-\zeta_\omega \omega_\omega T_s) \cos(\sqrt{1-\zeta_\omega^2}\omega_\omega T_s)]/T_s \\ k_{i,\omega} &= [\exp(-2\zeta_\omega \omega_\omega T_s) - 1]/T_s + k_{p,\omega} \end{aligned} \tag{27}$$

the poles of the angle-estimation loop have the natural frequency of ω_ω with the damping ratio of ζ_ω. The angle estimator is tuned via these parameters. The zero of the pulse-transfer function $G_\vartheta(z)$ introduces overshoot, e.g., in the case of step responses. Thus, it is beneficial to select a high damping ratio, e.g., $\zeta_\omega = 1$. The natural frequency ω_ω is directly related to the convergence speed of the angle tracking. For a step change in the angle, the estimation error is reduced below $\pm 5\%$ in $t_{5\%} \approx 4.2/\omega_\omega$, if $\zeta_\omega = 1$. Fig. 5(b) illustrates the response of the estimation error when a step change $\Delta\vartheta_g$ is applied in ϑ_g and the parameters are $\omega_\omega = 2\pi \cdot 50$ rad/s and $\omega_\omega = 2\pi \cdot 100$ rad/s. As the figure shows, the estimation error is practically zero after one 20-ms period of the grid voltage even for the smaller ω_ω.

According to (5), the relationship between the actual angle and angular frequency is $\vartheta_g(z) = [T_s/(z-1)]\omega_g(z)$. Since the estimator (7) corresponds to the actual dynamics (5), the linearized closed-loop transfer function $G_\omega(z) = \hat{\omega}_g(z)/\omega_g(z)$ for the frequency estimation equals (26). Fig. 6 shows the estimation-error response for the estimate $\hat{\omega}_g$. The settling time of $\hat{\omega}_g$ equals that of the angle $\hat{\vartheta}_g$ [cf. Fig 5(b)], since $G_\omega(z) = G_\vartheta(z)$.

Furthermore, the transfer function for the naturally filtered frequency estimate $\hat{\omega}_{gf}$ becomes

$$\begin{aligned} G_{\omega f}(z) &= \frac{\hat{\omega}_{gf}(z)}{\omega_g(z)} = \frac{F_{\omega f}(z)\frac{T_s}{z-1}}{1 + F_\omega(z)\frac{T_s}{z-1}} \\ &= \frac{k_{i,\omega} T_s}{z^2 + (k_{p,\omega}T_s - 2)z + k_{i,\omega}T_s - k_{p,\omega}T_s + 1} \end{aligned} \tag{28}$$

The estimation-error response of the estimate $\hat{\omega}_{gf}$ is also shown in Fig. 6. The error $\omega_g - \hat{\omega}_{gf}$ is reduced below $\pm 5\%$ in $t_{5\%} \approx 4.8/\omega_\omega$, if $\zeta_\omega = 1$. As the figure shows, also the estimation error $\omega_g - \hat{\omega}_{gf}$ of the naturally filtered frequency is practically zero after one 20-ms period of the grid voltage.

F. Small-Signal Stability

Tuning of the grid-voltage amplitude and angle estimators was based on the quasi-steady-state analysis, and the frequency-error-dependent part $\mathbf{\Gamma}_\omega$ of (12) was neglected. However, when the tuning parameters α_u and ω_ω (approximate bandwidths) approach the tuning parameters α_{od} and ω_{or} of the full-order observer, the quasi-steady-state assumption is not valid and the stability of the adaptive observer can be lost. In the following, the stability of the estimation scheme is further analyzed.

Considering (8), (12), and (21)–(23), the small-signal model for the closed-loop system is obtained and the estimation-error dynamics are[1]

$$\begin{cases} \tilde{\mathbf{x}}(k+1) = (\mathbf{\Phi} - \mathbf{K}_o\mathbf{C}_c)\,\tilde{\mathbf{x}}(k) + \mathrm{j}\mathbf{\Gamma}_g u_{g0}\tilde{\vartheta}_g(k) \\ \qquad\qquad + \mathbf{\Gamma}_\omega\tilde{\omega}_g(k) + \mathbf{\Gamma}_g\tilde{u}_g(k) \\ \tilde{u}_g(k+1) = \tilde{u}_g(k) - k_{i,u}\,\mathrm{Re}\left\{\frac{a}{b}\mathrm{e}^{\mathrm{j}\phi}\mathbf{C}_c\tilde{\mathbf{x}}(k)\right\} \\ \tilde{\omega}_{gf}(k+1) = \tilde{\omega}_{gf}(k) - \frac{k_{i,\omega}}{u_{g0}}\,\mathrm{Im}\left\{\frac{a}{b}\mathrm{e}^{\mathrm{j}\phi}\mathbf{C}_c\tilde{\mathbf{x}}(k)\right\} \\ \tilde{\vartheta}_g(k+1) = \tilde{\vartheta}_g(k) + T_s\tilde{\omega}_g(k) \end{cases} \tag{29}$$

where

$$\tilde{\omega}_g(k) = -\frac{k_{p,\omega}}{u_{g0}}\,\mathrm{Im}\left\{\frac{a}{b}\mathrm{e}^{\mathrm{j}\phi}\tilde{\boldsymbol{\imath}}_c(k)\right\} + \tilde{\omega}_{gf}(k) \tag{30}$$

The system is linear and its numerical analysis becomes straightforward, if the complex space vectors are written in component form.

The closed-loop stability of the entire observer is examined when the design parameters of the observer are altered. The nominal system parameters are given in Table I. The stability is analyzed numerically by calculating eigenvalues of the linearized system (29). Fig. 7 illustrates stability regions of

[1]For stability analysis, $\tilde{u}_g(k) = u_g(k) - \hat{u}_g(k)$, $\tilde{\omega}_{gf}(k) = \omega_g(k) - \hat{\omega}_{gf}(k)$, and $\tilde{\omega}_g(k) = \omega_g(k) - \hat{\omega}_g(k)$, where u_g and ω_g as external disturbances can be set to zero.

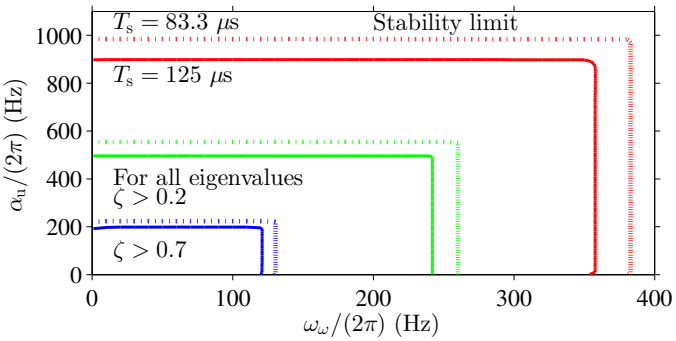

Fig. 7. Stability limits (red lines) of the adaptive observer as a function of the tuning parameters α_u and ω_ω when the other tuning parameters are: $\alpha_{od} = 2\pi \cdot 1200$ rad/s, $\omega_{or} = \omega_p$, $\zeta_{or} = 0.7$, and $\zeta_\omega = 1$. Two sampling periods are considered: $T_s = 125$ μs (solid lines) and $T_s = 83.3$ μs (dotted lines). Under the green lines, the damping ratios of the all eigenvalues are at least 0.2. Under the blue lines, the damping ratios are at least 0.7.

TABLE I
NOMINAL SYSTEM PARAMETERS

Param.	Value	Param.	Value
u_g	$\sqrt{2/3} \cdot 400$ V (1 p.u.)	L_{fc}	2.94 mH (0.072 p.u.)
ω_g	$2\pi \cdot 50$ rad/s	L_{fg}	1.96 mH (0.048 p.u.)
i_N	$\sqrt{2} \cdot 18$ A (1 p.u.)	C_f	10 μF (0.040 p.u.)
u_{dc}	650 V (2 p.u.)	ω_p	$2\pi \cdot 1470$ rad/s
f_{sw}	4 kHz	T_s	$1/(2f_{sw}) = 125$ μs

the closed-loop adaptive observer in the case of the different sampling periods $T_s = 83.3$ μH and $T_s = 125$ μH (corresponding the switching frequencies f_{sw} of 6 kHz and 4 kHz when two samples per switching period are taken). Moreover, the regions where the damping ratios of the all eigenvalues are at least 0.2 and 0.7 are illustrated. The figure shows that the eigenvalues are well damped if the tuning parameters of the adaptation loops α_u and ω_ω are selected a decade down from α_{od} and ω_{or}.

IV. UNBALANCED GRID CONDITIONS

A. Grid Voltage

Under unbalanced grid conditions (e.g. during single- and two-phase faults) the grid voltage vector (1) can be represented as

$$\boldsymbol{u}_g^s = e^{j\vartheta_{g+}} u_{g+} + e^{j\vartheta_{g-}} u_{g-} \tag{31}$$

where u_{g+} and u_{g-} are the magnitudes of the positive- and negative-sequence components, respectively. Furthermore, the positive-sequence angle is $\vartheta_{g+} = \int \omega_{g+} dt$, where ω_{g+} is the angular frequency of the positive sequence. The negative-sequence angle is $\vartheta_{g-} = -\int \omega_{g+} dt + \phi_{g-}$, where ϕ_{g-} is the phase shift of the negative-sequence component with respect to the positive-sequence component.

The observer presented in Section III estimates the angle ϑ_g of the vector $\boldsymbol{u}_g^s$. In balanced grid conditions, the angle equals the positive-sequence angle, i.e., $\vartheta_g = \vartheta_{g+}$. However under unbalanced conditions, the angle $\vartheta_g = \tan^{-1}(u_{g\beta}/u_{g\alpha})$ is [20]

$$\vartheta_g = \omega_{g+} t + \tan^{-1}\left[\frac{u_{g-}\sin(-2\omega_{g+}t + \phi_{g-})}{u_{g+} + u_{g-}\cos(-2\omega_{g+} + \phi_{g-})}\right] \tag{32}$$

Moreover, the angle is oscillating at the frequency components multiple to $2\omega_{g+}$ around the fundamental waveform $\omega_{g+}t$. The instantaneous angular frequency of the voltage vector $\boldsymbol{u}_g^s$ is

$$\frac{d\vartheta_g}{dt} = \frac{\omega_{g+}(u_{g+}^2 - u_{g-}^2)}{u_{g+}^2 + u_{g-}^2 + 2u_{g+}u_{g-}\cos(-2\omega_{g+}t + \phi_{g-})} \tag{33}$$

and the magnitude is

$$|\boldsymbol{u}_g^s| = \sqrt{u_{g+}^2 + u_{g-}^2 + 2u_{g+}u_{g-}\cos(2\omega_{g+}t - \phi_{g-})} \tag{34}$$

B. Improvement of the Positive-Sequence Tracking

According to (32)–(34), the frequency components multiple to $2\omega_{g+}$ are present in the instantaneous angle, frequency, and magnitude of $\boldsymbol{u}_g^s$ under unbalanced conditions. Tracking of these $2\omega_{g+}$ frequency components in the estimated quantities could be improved by increasing the bandwidths (tuning parameters α_u and ω_ω) of the adaptation loops. However, this would mean higher gains in the observer and it would decrease the robustness of the system. On the other hand, it is more convenient to modify the adaptation laws (21) and (22) to track the positive-sequence angle ϑ_{g+} and to reject the oscillations caused by the negative sequence.

In the case of phase-locked loops (PLLs), different types of filters and sequence separation strategies have been proposed in order to improve tracking of the positive-sequence angle of the grid-voltage under unbalanced conditions. For example, a notch filter or moving-average filter can be added to conventional PLLs [21]. Moreover, the moving-average filter or multiple notch filters in the loop improve disturbance rejection of the harmonics (e.g., 5th and 7th) of the grid voltage [21], [22].

Here, adding second-order notch filters into the adaptation loops is introduced as an option in order to improve disturbance rejection against the negative-sequence and harmonic-frequency components. The notch filter is

$$G_n(s) = \frac{s^2 + \omega_n^2}{s^2 + \frac{\omega_n}{Q}s + \omega_n^2} \tag{35}$$

where ω_n is the center (notch) frequency and Q is the quality factor that describes the selectivity of the filter. The bandwidth of the filter is $\alpha_n = \omega_n/Q$. The filter is discretized with Tustin's method and the pre-warping is used in order to correct the possibly warped center frequency. The pulse-transfer function of the discretized filter is

$$G_n(z) = \frac{c_{n1}(z^2 + c_{n2}z + 1)}{z^2 + c_{n1}c_{n2}z + 2c_{n1} - 1} \tag{36}$$

where the coefficients are

$$c_{n1} = \frac{2Q}{2Q + \sin(\omega_n T_s)}, \qquad c_{n2} = -2\cos(\omega_n T_s) \tag{37}$$

Fig. 8(a) shows the frequency response for the loop-transfer function of the magnitude adaptation loop (cf. Fig. 4), when the adaptation law (21) is cascaded with the notch filters $G_{n2\omega}(z)$ and $G_{n6\omega}(z)$ tuned at the center frequencies of $2\omega_g$ and $6\omega_g$, respectively. The bandwidths of the $2\omega_g$ and $6\omega_g$ notch filters are $2\pi \cdot 30$ rad/s and $2\pi \cdot 40$ rad/s, respectively. The zero gains at the frequencies of $2\omega_g$ and $6\omega_g$ indicate that

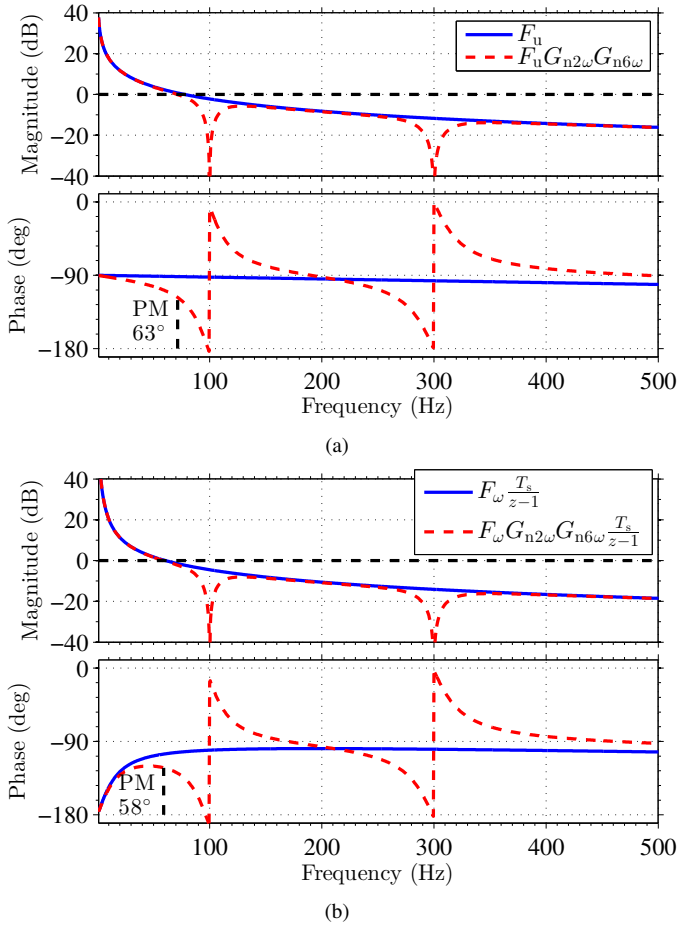

Fig. 8. Frequency responses. (a) Loop-transfer function of the magnitude adaptation loop: (blue) the adaptation law of (21) is used; (red) cascaded notch filters are used with the adaptation law. (b) Loop-transfer function of the angle and frequency adaptation loop: (blue) the adaptation law of (22) is used; (red) cascaded notch filters are used with the adaptation law.

the tracking of these frequencies is poor, which is desired. However, especially the notch filter at $2\omega_\mathrm{g}$ decreases the phase margin (PM) at the crossover frequency. Therefore, the bandwidth of the adaptation loop α_u has to be limited in order to provide a sufficient phase margin, e.g., 60°. Here, the bandwidth of $\alpha_\mathrm{u} = 2\pi \cdot 80$ rad/s is selected, which provides the phase margin of 63° as shown in the figure.

Fig. 8(b) shows the frequency response for the loop-transfer function of the angle adaptation loop (cf. Fig. 4), when the adaptation law (22) is cascaded with the same notch filters $G_{n2\omega}(z)$ and $G_{n6\omega}(z)$ tuned at the center frequencies of $2\omega_\mathrm{g}$ and $6\omega_\mathrm{g}$, respectively. Again, the notch filter at $2\omega_\mathrm{g}$ decreases the phase margin at the crossover frequency. Therefore, the tuning parameter ω_ω has to be limited in order to provide a sufficient phase margin. Here, $\omega_\omega = 2\pi \cdot 30$ rad/s is selected, which provides the phase margin of 58° as shown in the figure.

C. Modifications in the Control System

Different power control strategies in unbalanced grid conditions have been investigated, e.g., in [16]. The contribution of this paper is not in these control strategies, but, in order to study the performance of the proposed observer as a part of the control system, a strategy has to be selected. Here, the control structure is modified in order to produce balanced sinusoidal currents under unbalanced grid conditions. For this control strategy, two extensions are needed:

1) A possible double-fundamental-frequency ripple in the DC-link voltage is filtered in the voltage controller such that the ripple disappears from the power reference p_ref. A notch filter at $2\omega_\mathrm{g}$ is used.
2) The current controller is improved to reject the negative-sequence disturbance.

The negative sequence of the grid voltage together with the grid-voltage harmonics are disturbances for the current controller. In order to improve disturbance rejection, generalized integrators at the disturbance frequencies have been added in the current control algorithm similarly to [23], [24]. The state-space current controller proposed in [18] is used in this work. For regulation of m harmonic sequences ($m = \ldots -6, -2, 6, \ldots$) at the synchronous reference frame, the current controller is augmented with additional integrating states

$$\boldsymbol{x}_{\mathrm{I},m}(k+1) = \mathrm{e}^{\mathrm{j}m\omega_\mathrm{g}T_\mathrm{s}}\boldsymbol{x}_{\mathrm{I},m}(k) + \boldsymbol{i}_{\mathrm{c,ref}}(k) - \boldsymbol{i}_\mathrm{c}(k) \qquad (38)$$

where $\boldsymbol{i}_{\mathrm{c,ref}}$ is the current reference. These integral states are often referred to as reduced-order generalized integrators (ROGIs) [23]. The augmented control law is

$$\boldsymbol{u}'_{\mathrm{c,ref}}(k) = \boldsymbol{u}_{\mathrm{c,ref}}(k) + \sum_m \boldsymbol{k}_{\mathrm{I},m}\boldsymbol{x}_{\mathrm{I},m}(k) \qquad (39)$$

where $\boldsymbol{u}_{\mathrm{c,ref}}(k)$ is the control voltage of the original controller [18] and $\boldsymbol{k}_{\mathrm{I},m}$ is the gain for the m-harmonic integrator.

V. Comparison Between the Proposed Method and Its Continuous-Time Counterpart

An alternative for the proposed direct discrete-time design method is the continuous-time design method with an approximate discretization for digital implementation [12]. In comparison with the direct discrete-time design, the continuous-time design is often easier and the models, e.g., system matrices, are simpler. However, the complexity of the continuous design is hidden in the digital implementation. For the full-order observer in [12], Tustin's method for the discretization is needed, which makes updating and computing the discrete approximation of the continuous-time observer at least as time-consuming as updating the proposed observer.

In order to compare the proposed observer and its continuous-time counterpart [12], the both observer designs were first simulated in the case of the nominal system parameters, cf. Table I. To equalize the test conditions, the both observers were simultaneously running in parallel with a control system. Fig. 9(a) shows the simulated responses of the estimation error when the converter current $\boldsymbol{i}^\mathrm{g}_\mathrm{c}$ (in the actual grid-voltage coordinates) was stepwise changed from $i^\mathrm{g}_\mathrm{cd} = 1.5$ p.u. to $i^\mathrm{g}_\mathrm{cd} = -1.5$ p.u. The both observers operate as designed and the steady-state errors are zero. The tuning parameters of the full-order observers correspond to Fig. 7: $\alpha_\mathrm{od} = 2\pi \cdot 1200$ rad/s, $\omega_\mathrm{or} = \omega_\mathrm{p}$, and $\zeta_\mathrm{or} = 0.7$. The tuning parameters for the adaptation loops are: $\alpha_\mathrm{u} = 2\pi \cdot 100$ rad/s,

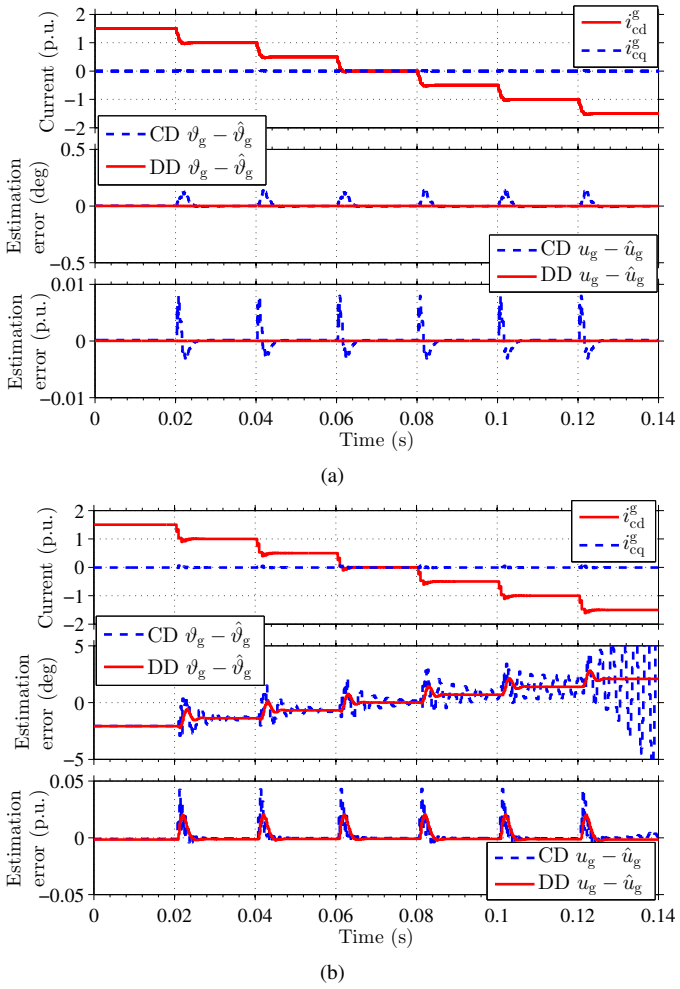

Fig. 9. Simulated estimation-error responses of the proposed observer (DD) and its continuous-time counterpart (CD, dashed line) when the operating point is changing: (a) the system parameters are nominal, and the sampling time of the both observers is $T_{\mathrm{s}} = 125$ μs; (b) the model parameters of the observers are erroneous (true L_{fg} is 50% larger than the nominal L_{fg} used in the observers), the sampling time is $T_{\mathrm{s}} = 250$ μs, and the tuning parameter ω_ω is increased to $2\pi \cdot 150$ rad/s. Note that the scales of the y-axes of the subfigures (a) and (b) are not equal.

$\omega_\omega = 2\pi \cdot 50$ rad/s, and $\zeta_\omega = 1$. All the tuning parameters, including the sampling time $T_{\mathrm{s}} = 125$ μs, are the same for the both observers under comparison.

Fig. 9(b) shows the estimation-error responses in the case of the erroneous parameters and a longer sampling time. For the both observers under comparison, the sampling time is doubled to $T_{\mathrm{s}} = 250$ μs which corresponds the switching frequency of 4 kHz with once-per-carrier synchronous sampling. The tuning parameter of the angle estimator is increased to $\omega_\omega = 2\pi \cdot 150$ rad/s for faster tracking of the grid-voltage angle. Moreover, the model parameters of the both observers are erroneous: the real grid-side inductance L_{fg} is increased by 50% while the model parameters in the observers are nominal. As the figure shows, the observer designed in the continuous-time domain (blue dashed line) becomes unstable, whereas the proposed observer (red solid line) is fully operational. Steady-state estimation errors depend on the operating point. The results indicate that the proposed direct digital design works better than the continuous-time design at low sampling frequencies. Naturally, when the sampling frequency is higher, the functional difference between the compared methods is smaller.

VI. Experimental Results

A. Validation

The proposed adaptive observer was experimentally tested as a part of a grid-voltage sensorless control scheme shown in Fig. 1(b). The switching frequency of the 12.5-kVA, 400-V converter under test was 4 kHz and synchronous sampling (twice-per carrier) was used. The converter was connected to the electric power distribution system via a 1-MVA 20-kV/400-V transformer. The nominal system parameters are given in Table I. State-space current control [18], designed in the discrete-time domain, was used and the control algorithm was implemented on dSPACE DS1006 processor board. The converter under test was regulating the dc-bus voltage u_{dc} whereas another back-to-back connected converter was feeding power to the bus.

The current controller was tuned to give an approximate closed-loop bandwidth of 600 Hz. Either nominal u_{g} or estimated and filtered $\hat{u}_{\mathrm{g}}$ can be used in the current reference calculation, cf. Fig 1(b). The nominal value is used in this paper. The dominant estimation-error dynamics were set twice as fast as the current-control bandwidth, i.e., $\alpha_{\mathrm{od}} = 2\pi \cdot 1200$ rad/s. The undamped natural frequency ω_{or} was set to the resonance frequency ω_{p} with the damping ratio of $\zeta_{\mathrm{or}} = 0.7$. The tuning parameters for the adaptation loops were: $\alpha_{\mathrm{u}} = 2\pi \cdot 100$ rad/s, $\omega_\omega = 2\pi \cdot 50$ rad/s, and $\zeta_\omega = 1$.

1) Angle Tracking: Fig. 10(a) shows the responses of the estimated and actual grid-voltage angles when the impulse disturbance of $+60^\circ$ was applied into the estimated angle $\hat{\vartheta}_{\mathrm{g}}$. At the same time, the converter was supplying the power of 0.4 p.u. to the grid. Fig. 10(b) compares the measured angle-estimation error with the corresponding theoretical estimation error that is obtained from (29). As can be seen from the figure, the agreement between theoretical and measured estimation errors is good. Moreover, the designed dynamic behavior is realized, cf. Fig. 5(b). The small 300-Hz ripple in the measured estimation error originates from the grid-voltage harmonics.

2) Magnitude Tracking: Fig. 11(a) shows the responses of the estimated and actual grid-voltage magnitudes when the impulse disturbance of -0.9 p.u. was applied into the estimated magnitude $\hat{u}_{\mathrm{g}}$. At the same time, the converter was supplying the power of 0.4 p.u. to the grid. Fig. 11(b) compares the measured waveform of the magnitude-estimation error with the theoretical estimation error that is obtained from (29). As the figure shows, the agreement between the theoretical response and measurement is good. Furthermore, the measured estimation-error dynamics correspond to the designed dynamics, cf. Fig. 5(a).

3) Frequency Tracking: Fig. 12(a) shows the responses of the estimated and actual grid-voltage frequencies when the impulse disturbance of -10 Hz was applied into the estimated frequency $\hat{\omega}_{\mathrm{gf}}$. At the same time, the converter was supplying the power of 0.4 p.u. to the grid. Fig. 12(b)

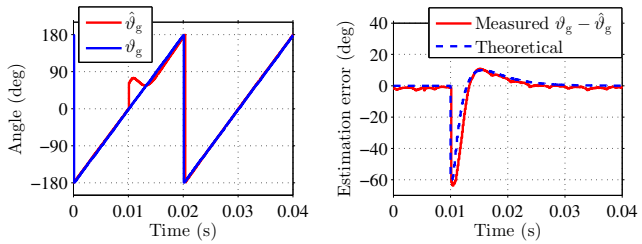

Fig. 10. Experimental results when the disturbance impulse of $+60$ degrees is applied into the estimated grid-voltage angle: (a) estimated and actual angles; (b) measured angle-estimation error and corresponding theoretical response from (29).

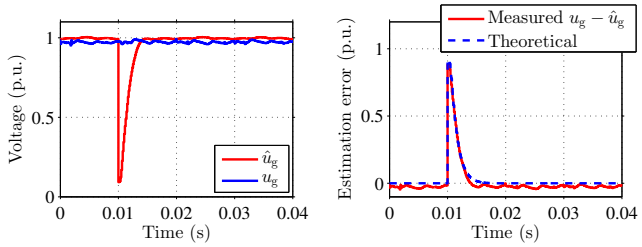

Fig. 11. Experimental results when the disturbance impulse of -0.9 p.u. is applied into the estimated grid-voltage magnitude: (a) estimated and actual magnitudes; (b) measured magnitude-estimation error and corresponding theoretical response from (29).

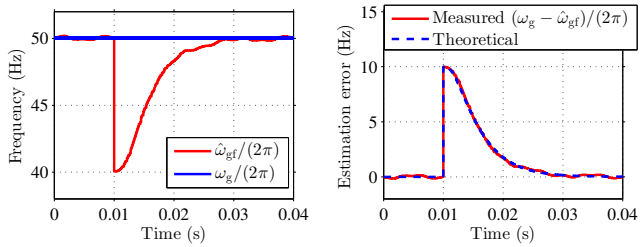

Fig. 12. Experimental results when the disturbance impulse of -10 Hz is applied into the estimated grid-voltage frequency: (a) estimated and actual frequencies; (b) measured frequency-estimation error and corresponding theoretical response from (29).

compares the measured waveform of the frequency-estimation error with the theoretical estimation error that is obtained from (29). As the figure shows, the agreement between the theoretical response and measurement is good. Furthermore, the measured estimation-error dynamics agree well with the designed dynamics, cf. Fig. 6.

B. Operation Under Balanced Grid Disturbances

Operation of the grid-voltage sensorless control scheme was tested under grid-voltage dips, phase-angle jumps and frequency changes. The disturbances were supplied using a 50-kVA three-phase four-quadrant power supply (Regatron TopCon TC.ACS).

1) Grid-Voltage Dip: Operation under a grid-voltage dip of 0.5 p.u. was evaluated. The converter was supplying the power of 0.5 p.u. to the grid. The measured responses of the

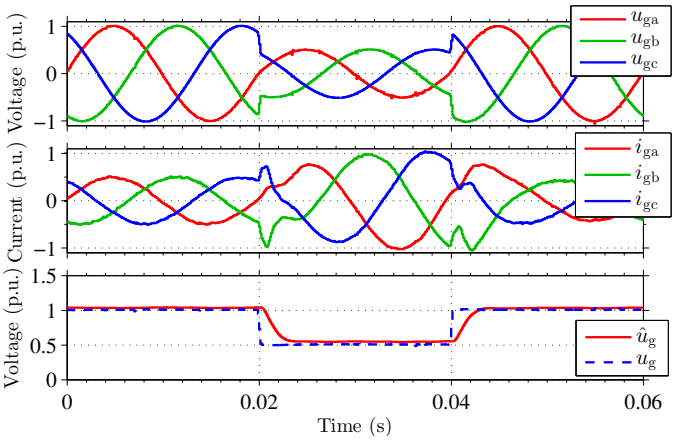

Fig. 13. Measured grid voltages u_{ga}, u_{gb}, and u_{gc} (above), grid currents i_{ga}, i_{gb}, and i_{gc} (middle), and the estimated and actual grid-voltage magnitudes (below), when a grid-voltage dip is applied.

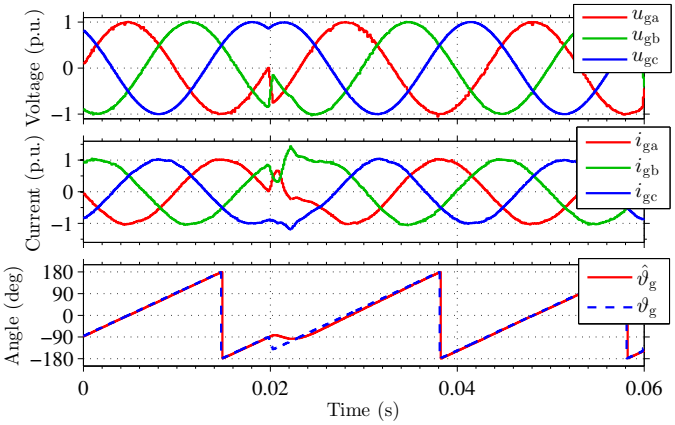

Fig. 14. Measured grid voltages u_{ga}, u_{gb}, and u_{gc} (above), grid currents i_{ga}, i_{gb}, and i_{gc} (middle), and the estimated and actual grid-voltage angles (below), when a grid-voltage angle is changing rapidly $-60°$.

estimated grid-voltage magnitude and the grid currents i_{ga}, i_{gb}, and i_{gc} are shown in Fig. 13. As the figure shows, the estimated magnitude $\hat{u}_g$ rapidly follows the actual magnitude. The steady-state estimation error is small (0.03 p.u.) and it is explained by parameter uncertainties of the experimental setup.

During the dip, the currents rises to 1 p.u. since the power of 0.5 p.u. has to be transferred. Naturally, if the load power of 1 p.u. were transferred, the currents would rise to 2 p.u. during the dips. This would trigger the over-current limit of the converter, if the limit were, e.g., 1.5 p.u. However, the currents can be temporarily limited by the controller and the energy that the converter cannot transfer during the dips could be supplied or drawn by DC-link capacitors.

2) Phase-Angle Jump: When the converter was rectifying the power of -1 p.u. from the grid, the grid-voltage angle was rapidly changed $-60°$. Fig. 14 shows the measured responses of the grid currents and the estimated and actual grid-voltage angles. As the figure shows, the estimated angle $\hat{\vartheta}_g$ rapidly follows the actual angle and the steady-state operation is achieved in a half cycle of the grid voltage. The steady-state estimation error of the angle is $1.5°$, which causes only a small

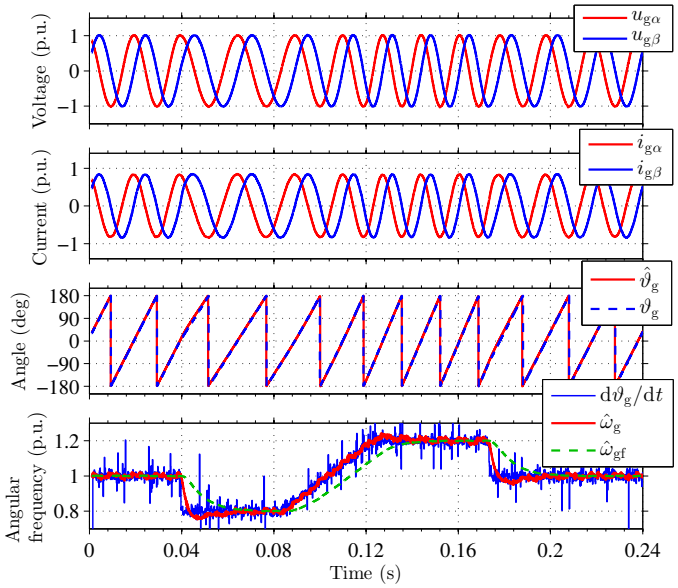

Fig. 15. Measured space-vector components of the grid voltage (first), the space-vector components of the grid current (second), the estimated and actual grid-voltage angles (third), estimated angular frequencies $\hat{\omega}_\mathrm{g}$ and $\hat{\omega}_\mathrm{gf}$, and actual grid-voltage frequency (fourth), when the frequency is changing. The actual frequency $\omega_\mathrm{g} = \mathrm{d}\vartheta_\mathrm{g}/\mathrm{d}t$ is noisy since it is calculated by differentiating the actual angle $\vartheta_\mathrm{g} = \tan^{-1}(u_{\mathrm{g}\beta}/u_{\mathrm{g}\alpha})$.

error $[1 - \cos(1.5°) = 0.0003]$ in the power factor.

3) Grid-Frequency Perturbation: When the converter was supplying the power of 0.8 p.u. to the grid, the grid-voltage frequency was stepwise changed from 50 Hz (1 p.u.) to 40 Hz. Then, the frequency of the voltage was ramped up to 60 Hz and stepwise changed back to 50 Hz. Fig. 15 shows the measured responses of the grid-current components $i_{\mathrm{g}\alpha}$ and $i_{\mathrm{g}\beta}$, the estimated and actual grid-voltage angles, and the estimated and actual grid-voltage frequencies. The estimate $\hat{\omega}_\mathrm{g}$ converges quickly, but includes some noise. On the other hand, the estimate $\hat{\omega}_\mathrm{gf}$ (dashed line) converges a bit slower, as also predicted in Fig. 6, but it is free of noise and, therefore, more suitable for monitoring purposes. Moreover, the proposed sensorless control system can operate with different frequencies without difficulties and its naturally frequency adaptable as the transferred grid currents illustrate.

C. Operation In Unbalanced and Distorted Grid Conditions

The operation of the sensorless control system under unbalanced and distorted grid conditions was tested. The distorted voltage were supplied using the 50-kVA Regatron power supply.

1) Distorted Grid Conditions: Fig. 16 illustrates conditions, when there is unbalance in the grid voltages ($u_\mathrm{ga} = 0.9$ p.u., $u_\mathrm{gb} = 1$ p.u., and $u_\mathrm{gc} = 1.1$ p.u.). The phase voltages contain the 5th and 7th harmonic components, whose magnitudes are 0.05 p.u. The converter is supplying the power of 1 p.u. At $t = 0 \ldots 0.04$ s, the observer design described in Section III is used. Clearly, the grid currents are distorted and the estimated magnitude, frequency, and angle contain harmonic components at $2\omega_\mathrm{g}$ and $6\omega_\mathrm{g}$. Moreover, the total harmonic distortion (THD) up to the 50th order of the currents is THD $= 17.4\%$.

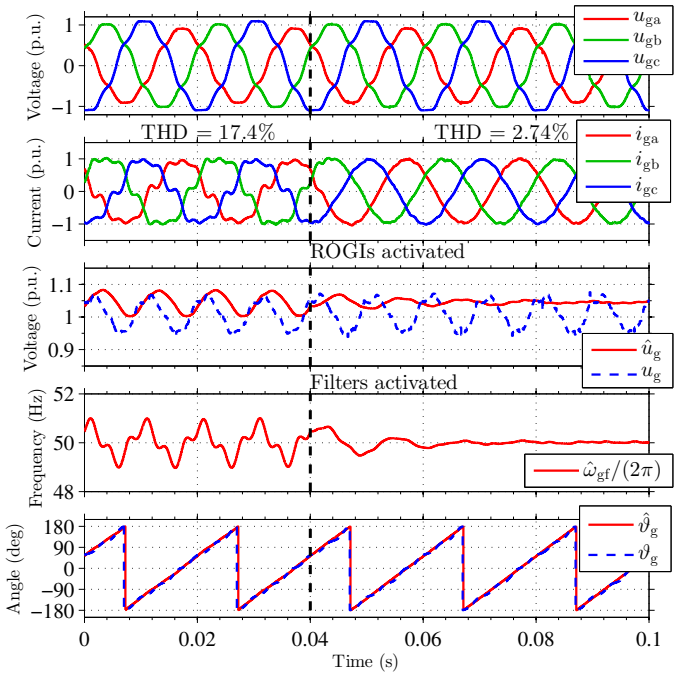

Fig. 16. Measured three-phase grid voltages (first), three-phase grid currents (second), the estimated and actual grid-voltage magnitudes (third), estimated angular frequency $\hat{\omega}_\mathrm{gf}$ (fourth), and estimated and actual grid-voltage angles (fifth), when the grid voltages are distorted and unbalanced. After $t = 0.04$ s, generalized integrators in the current controller and the notch filters in the adaptation loops and DC-voltage control are activated.

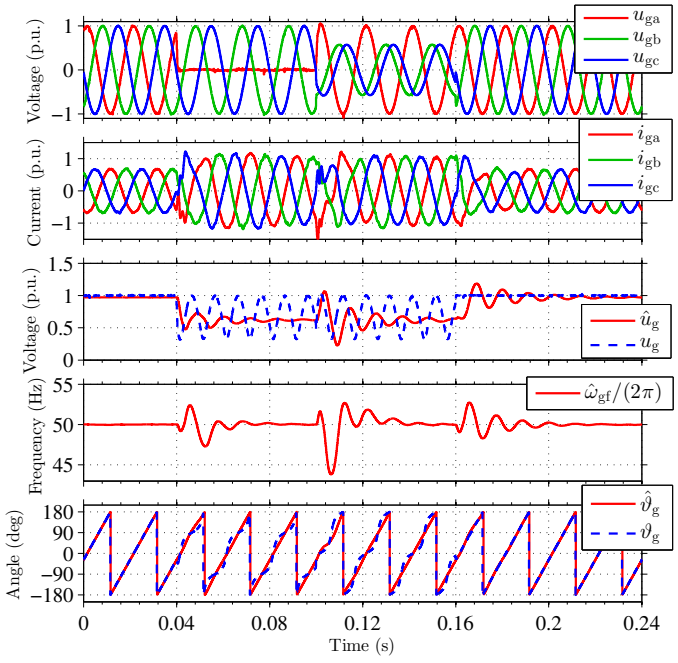

Fig. 17. Measured three-phase grid voltages (first), three-phase grid currents (second), the estimated and actual grid-voltage magnitudes (third), estimated angular frequency $\hat{\omega}_\mathrm{gf}$ (fourth), and estimated and actual grid-voltage angles (fifth), when unbalanced grid-voltage dips are applied.

The improvements for the distorted and unbalanced conditions described in Section IV are enabled at $t = 0.04$ s. In other words, the notch filters at $2\omega_\mathrm{g}$ and $6\omega_\mathrm{g}$ are activated in the adaptation loops, $2\omega_\mathrm{g}$ oscillations from the power

reference p_{ref} are filtered in DC-link voltage control, and the ROGIs at $2\omega_{\mathrm{g}}$ and $\pm 6\omega_{\mathrm{g}}$ are activated in current control. It can be seen that the harmonic oscillations disappear from the estimated quantities and the grid currents become less distorted. Moreover, the THD up to the 50th order of the currents is THD $= 2.74\%$.

The steady-state estimation error in the grid-voltage magnitude is 0.041 p.u., which originates from uncertainties in the experimental setup that are not explained by the model (4). For example, the series resistances of the inductors cause a bias in the estimated magnitude, which approximately equals the voltage drop in the resistors. The total DC resistance in the filter inductors is $R = 0.17\ \Omega$ (0.013 p.u.). Including the resistances in the model (4) would increase its complexity.

2) Unbalanced Grid-Voltage Dips: The improvements for the distorted and unbalanced conditions described in Section IV are used. Operation under the single-phase dip (line-to-ground fault) down to zero is illustrated in Fig. 17. After the single-phase dip, a two-phase dip down to 0.58 p.u. is applied at 0.1 s. This dip corresponds to the single-phase dip transformed through a Dy transformer [25]. Finally, the grid voltages return back to their normal balanced conditions. During the dips, the converter is rectifying the power of 0.67 p.u.

As Fig. 17 shows, the notch filters attenuate the $2\omega_{\mathrm{g}}$ oscillations in the estimated magnitude, frequency, and angle. The estimated angle follows the positive-sequence angle of the grid voltage. The positive-sequence magnitude is 0.67 p.u. during the dips, and the estimated magnitude converges close to that value (0.62 p.u.).

The sensorless control system is operating well. The magnitudes of the currents increase to 1 p.u during the dips in order transfer the load power of 0.67 p.u. Moreover, the grid currents are balanced in steady state. The highest current peak in transients is -1.5 p.u, which is close to the over-current limit of the converter. However, the presented synthetic voltage transients are fast and among the worst-case scenarios. Naturally, if the load power of 1 p.u. were transferred before the presented dips, the currents would rise to 1.5. p.u. in steady state during the dips and possibly even higher in the transients. Therefore, the over-current rating of the converter should be increased, if the full load-power transfer of 1 p.u. is required during the presented dips.

VII. Conclusion

This paper presents a discrete-time adaptive full-order observer for grid-voltage sensorless control of a grid-connected converter equipped with an LCL filter. The proposed analytical design method gives simple expressions for the gains of the observer scheme. The implementation of the method is straightforward following directly from the digital design. According to the simulations, the proposed method suits low sampling rates better than its continuous-time counterpart. The proposed oberver is experimentally tested as a part of a grid-voltage sensorless control system. Experimental results confirm the design method and indicate fast tracking of the grid-voltage magnitude, frequency, and angle. Moreover, the proposed observer can operate in distorted and unbalanced grid conditions. Tracking of the positive-sequence component of the grid-voltage is achieved by using notch filters in the magnitude and frequency estimators. Grid-voltage sensorless control provides redundancy in the case of sensor faults or cost savings when the voltage sensors can be eliminated. The proposed design could be applied, e.g., in active-front-end rectifiers of motor drives.

Appendix A
Parameters of the Discretized System

The state-transition matrix $\boldsymbol{\Phi}$ in (4) is

$$\boldsymbol{\Phi} = \boldsymbol{\gamma}\begin{bmatrix} \frac{L_{\mathrm{fc}}+L_{\mathrm{fg}}\cos(\omega_{\mathrm{p}}T_{\mathrm{s}})}{L_{\mathrm{t}}} & -\frac{\sin(\omega_{\mathrm{p}}T_{\mathrm{s}})}{\omega_{\mathrm{p}}L_{\mathrm{fc}}} & \frac{L_{\mathrm{fg}}[1-\cos(\omega_{\mathrm{p}}T_{\mathrm{s}})]}{L_{\mathrm{t}}} \\ \frac{\sin(\omega_{\mathrm{p}}T_{\mathrm{s}})}{\omega_{\mathrm{p}}C_{\mathrm{f}}} & \cos(\omega_{\mathrm{p}}T_{\mathrm{s}}) & -\frac{\sin(\omega_{\mathrm{p}}T_{\mathrm{s}})}{\omega_{\mathrm{p}}C_{\mathrm{f}}} \\ \frac{L_{\mathrm{fc}}[1-\cos(\omega_{\mathrm{p}}T_{\mathrm{s}})]}{L_{\mathrm{t}}} & \frac{\sin(\omega_{\mathrm{p}}T_{\mathrm{s}})}{\omega_{\mathrm{p}}L_{\mathrm{fg}}} & \frac{[L_{\mathrm{fg}}+L_{\mathrm{fc}}\cos(\omega_{\mathrm{p}}T_{\mathrm{s}})]}{L_{\mathrm{t}}} \end{bmatrix} \tag{40}$$

where $\boldsymbol{\gamma} = \mathrm{e}^{-\mathrm{j}\omega_{\mathrm{g}}T_{\mathrm{s}}}$, $L_{\mathrm{t}} = L_{\mathrm{fc}} + L_{\mathrm{fg}}$ and ω_{p} is the resonance frequency (3) of the LCL filter. The input vector for the converter voltage in (4) is

$$\boldsymbol{\Gamma}_{\mathrm{c}} = \boldsymbol{\gamma}\begin{bmatrix} \frac{T_{\mathrm{s}}}{L_{\mathrm{t}}} + \frac{L_{\mathrm{fg}}\sin(\omega_{\mathrm{p}}T_{\mathrm{s}})}{\omega_{\mathrm{p}}L_{\mathrm{fc}}L_{\mathrm{t}}} \\ \frac{L_{\mathrm{fg}}[1-\cos(\omega_{\mathrm{p}}T_{\mathrm{s}})]}{L_{\mathrm{t}}} \\ \frac{T_{\mathrm{s}}}{L_{\mathrm{t}}} - \frac{\sin(\omega_{\mathrm{p}}T_{\mathrm{s}})}{\omega_{\mathrm{p}}L_{\mathrm{t}}} \end{bmatrix} \tag{41}$$

The elements of the input vector for the grid voltage $\boldsymbol{\Gamma}_{\mathrm{g}} = [\boldsymbol{b}_{\mathrm{g}1}\ \boldsymbol{b}_{\mathrm{g}2}\ \boldsymbol{b}_{\mathrm{g}3}]^{\mathrm{T}}$ in (4) are

$$\begin{aligned} \boldsymbol{b}_{\mathrm{g}1} &= \frac{\boldsymbol{\gamma}\left[-\omega_{\mathrm{g}}\omega_{\mathrm{p}}\sin(\omega_{\mathrm{p}}T_{\mathrm{s}}) + \mathrm{j}\omega_{\mathrm{g}}^2\cos(\omega_{\mathrm{p}}T_{\mathrm{s}}) - \mathrm{j}\rho\right] - \mathrm{j}\omega_{\mathrm{p}}^2}{\rho\omega_{\mathrm{g}}(L_{\mathrm{fc}}+L_{\mathrm{fg}})} \\ \boldsymbol{b}_{\mathrm{g}2} &= \frac{\boldsymbol{\gamma}\left[\omega_{\mathrm{p}}\cos(\omega_{\mathrm{p}}T_{\mathrm{s}}) + \mathrm{j}\omega_{\mathrm{g}}\sin(\omega_{\mathrm{p}}T_{\mathrm{s}})\right] - \omega_{\mathrm{p}}}{\rho\omega_{\mathrm{p}}C_{\mathrm{f}}L_{\mathrm{fg}}} \\ \boldsymbol{b}_{\mathrm{g}3} &= \boldsymbol{\gamma}\frac{\omega_{\mathrm{g}}\omega_{\mathrm{p}}L_{\mathrm{fc}}\sin(\omega_{\mathrm{p}}T_{\mathrm{s}}) - \mathrm{j}\rho L_{\mathrm{fg}} - \mathrm{j}\omega_{\mathrm{g}}^2L_{\mathrm{fc}}\cos(\omega_{\mathrm{p}}T_{\mathrm{s}})}{\rho\omega_{\mathrm{g}}L_{\mathrm{fg}}(L_{\mathrm{fc}}+L_{\mathrm{fg}})} \\ &\quad + \frac{\mathrm{j}\rho L_{\mathrm{fg}} + \mathrm{j}\omega_{\mathrm{g}}^2L_{\mathrm{fc}}}{\rho\omega_{\mathrm{g}}L_{\mathrm{fg}}(L_{\mathrm{fc}}+L_{\mathrm{fg}})}, \end{aligned} \tag{42}$$

where $\rho = \omega_{\mathrm{g}}^2 - \omega_{\mathrm{p}}^2$.

Appendix B
Small-Signal Linearization of the Estimation-Error Dynamics

When the stable operation of the observer is assumed, the nonlinear estimation-error dynamics (11)

$$\tilde{\mathbf{x}}(k+1) = \boldsymbol{f}[\tilde{\mathbf{x}}(k), \mathbf{x}(k), \boldsymbol{u}_{\mathrm{c}}(k), u_{\mathrm{g}}(k), \tilde{u}_{\mathrm{g}}(k), \tilde{\vartheta}_{\mathrm{g}}(k), \tilde{\omega}_{\mathrm{g}}(k)] \tag{43}$$

have an equilibrium point (marked with the subscript 0)

$$\tilde{\mathbf{x}}_0 = \boldsymbol{f}[\tilde{\mathbf{x}}_0, \mathbf{x}_0, \boldsymbol{u}_{\mathrm{c}0}, u_{\mathrm{g}0}, \tilde{u}_{\mathrm{g}0}, \tilde{\vartheta}_{\mathrm{g}0}, \tilde{\omega}_{\mathrm{g}0}] \tag{44}$$

If the circuit parameters are accurate ($\hat{L}_{\mathrm{fg}} = L_{\mathrm{fc}}$, $\hat{C}_{\mathrm{f}} = C_{\mathrm{f}}, \hat{L}_{\mathrm{fg}} = L_{\mathrm{fg}}$) in the observer matrices and the frequency estimation error is zero ($\tilde{\omega}_{\mathrm{g}0} = \omega_{\mathrm{g}0} - \hat{\omega}_{\mathrm{g}0} = 0$), the system matrices are equal $\hat{\boldsymbol{\Phi}}_0 = \boldsymbol{\Phi}_0$, $\hat{\boldsymbol{\Gamma}}_{\mathrm{c}0} = \boldsymbol{\Gamma}_{\mathrm{c}0}$, and $\hat{\boldsymbol{\Gamma}}_{\mathrm{g}0} = \boldsymbol{\Gamma}_{\mathrm{g}0}$. It follows that the estimation errors are zero $\{\tilde{\mathbf{x}}_0 = 0,\ \tilde{u}_{\mathrm{g}0} = 0,$

$\tilde{\omega}_{\mathrm{g}0} = 0,\ \tilde{\vartheta}_{\mathrm{g}0} = 0\}$ at the equilibrium point with the accurate parameters. In the vicinity of the equilibrium, the small-signal deviation is marked with δ, e.g., $\delta\tilde{\vartheta}_{\mathrm{g}} = \tilde{\vartheta}_{\mathrm{g}} - \tilde{\vartheta}_{\mathrm{g}0}$. In terms of the small-signal deviations, the estimation error dynamics around the equilibrium are

$$\begin{aligned}\delta\tilde{\mathbf{x}}(k+1) = &\left(\frac{\partial \boldsymbol{f}}{\partial \tilde{\mathbf{x}}}\right)_0 \delta\tilde{\mathbf{x}}(k) + \left(\frac{\partial \boldsymbol{f}}{\partial \mathbf{x}}\right)_0 \delta\mathbf{x}(k) \\ &+ \left(\frac{\partial \boldsymbol{f}}{\partial \boldsymbol{u}_{\mathrm{c}}}\right)_0 \delta\boldsymbol{u}_{\mathrm{c}}(k) + \left(\frac{\partial \boldsymbol{f}}{\partial u_{\mathrm{g}}}\right)_0 \delta u_{\mathrm{g}}(k) \\ &+ \left(\frac{\partial \boldsymbol{f}}{\partial \tilde{u}_{\mathrm{g}}}\right)_0 \delta\tilde{u}_{\mathrm{g}}(k) + \left(\frac{\partial \boldsymbol{f}}{\partial \tilde{\vartheta}_{\mathrm{g}}}\right)_0 \delta\tilde{\vartheta}_{\mathrm{g}}(k) \\ &+ \left(\frac{\partial \boldsymbol{f}}{\partial \tilde{\omega}_{\mathrm{g}}}\right)_0 \delta\tilde{\omega}_{\mathrm{g}}(k)\end{aligned} \tag{45}$$

when constant ω_{g} is assumed, i.e., $\delta\omega_{\mathrm{g}} = 0$. All the partial derivatives are evaluated at the equilibrium point, and they are

$$\begin{aligned}&\left(\frac{\partial \boldsymbol{f}}{\partial \tilde{\mathbf{x}}}\right)_0 = \boldsymbol{\Phi}_0 - \mathbf{K}_{\mathrm{o}}\mathbf{C}_{\mathrm{c}} \\ &\left(\frac{\partial \boldsymbol{f}}{\partial \mathbf{x}}\right)_0 = \left(\frac{\partial \boldsymbol{f}}{\partial \boldsymbol{u}_{\mathrm{c}}}\right)_0 = \left(\frac{\partial \boldsymbol{f}}{\partial u_{\mathrm{g}}}\right)_0 = 0 \\ &\left(\frac{\partial \boldsymbol{f}}{\partial \tilde{u}_{\mathrm{g}}}\right)_0 = \boldsymbol{\Gamma}_{\mathrm{g}0}, \qquad \left(\frac{\partial \boldsymbol{f}}{\partial \tilde{\vartheta}_{\mathrm{g}}}\right)_0 = \mathrm{j}u_{\mathrm{g}0}\boldsymbol{\Gamma}_{\mathrm{g}0} \\ &\left(\frac{\partial \boldsymbol{f}}{\partial \tilde{\omega}_{\mathrm{g}}}\right)_0 = \left[\mathrm{j}\boldsymbol{\Gamma}_{\mathrm{g}0}T_{\mathrm{s}} - \left(\frac{\mathrm{d}\hat{\boldsymbol{\Gamma}}_{\mathrm{g}}}{\mathrm{d}\tilde{\omega}_{\mathrm{g}}}\right)_0\right] u_{\mathrm{g}0}\end{aligned} \tag{46}$$

It is to be noted that the observer system matrices $\hat{\boldsymbol{\Phi}}$, $\hat{\boldsymbol{\Gamma}}_{\mathrm{c}}$, and $\hat{\boldsymbol{\Gamma}}_{\mathrm{g}}$ correspond to $\boldsymbol{\Phi}$, $\boldsymbol{\Gamma}_{\mathrm{c}}$, and $\boldsymbol{\Gamma}_{\mathrm{g}}$, but they are functions of $\hat{\omega}_{\mathrm{g}}$ instead of ω_{g}. Thus, they are functions of $\tilde{\omega}_{\mathrm{g}} = \omega_{\mathrm{g}} - \hat{\omega}_{\mathrm{g}}$ and their partial derivatives are considered with respect to $\tilde{\omega}_{\mathrm{g}}$ in (46). In order to shorten notation, δ is left out in the resulting linearized dynamics (12) and in Section III.

ACKNOWLEDGMENT

The authors would like to thank ABB Oy, Finnish Foundation for Technology Promotion, and the Emil Aaltonen Foundation for the financial support.

REFERENCES

[1] *IEEE Standard for Interconnecting Distributed Resources with Electric Power Systems*, IEEE Std. 1547-2003, Jul. 2003.

[2] K. Jalili and S. Bernet, "Design of LCL filters of active-front-end two-level voltage-source converters," *IEEE Trans. Ind. Electron.*, vol. 56, no. 5, pp. 1674–1689, May 2009.

[3] F. Betin, G.-A. Capolino, D. Casadei, B. Kawkabani, R. I. Bojoi, L. Harnefors, E. Levi, L. Parsa, and B. Fahimi, "Trends in electrical machines control: Samples for classical, sensorless, and fault-tolerant techniques," *IEEE Ind. Electron. Mag.*, vol. 8, no. 2, pp. 43–55, Jun. 2014.

[4] M. Malinowski and S. Bernet, "A simple voltage sensorless active damping scheme for three-phase PWM converters with an LCL filter," *IEEE Trans. Ind. Electron.*, vol. 55, no. 4, pp. 1876–1880, Apr. 2008.

[5] Fraunhofer ISE. (2015) Current and future cost of photovoltaics. long-term scenarios for market development, system prices and LCOE of utility-scale PV systems. Study on behalf of Agora Energiewende. [Online]. Available: www.agora-energiewende.de

[6] L. A. Serpa, S. Ponnaluri, P. M. Barbosa, and J. W. Kolar, "A modified direct power control strategy allowing the connection of three-phase inverters to the grid through LCL filters," *IEEE Trans. Ind. Appl.*, vol. 43, no. 5, pp. 1388–1400, Sep./Oct. 2007.

[7] G. Wrona and K. Malon, "Sensorless operation of an active front end converter with LCL filter," in *Proc. ISIE 2014*, Istanbul, Turkey, Jun. 2014, pp. 2697–2702.

[8] B. Bolsens, K. De Brabandere, J. Van den Keybus, J. Driesen, and R. Belmans, "Model-based generation of low distortion currents in grid-coupled PWM-inverters using an LCL output filter," *IEEE Trans. Power Electron.*, vol. 21, no. 4, pp. 1032–1040, Jul. 2006.

[9] K. H. Ahmed, A. M. Massoud, S. J. Finney, and B. W. Williams, "Sensorless current control of three-phase inverter-based distributed generation," *IEEE Trans. Power Del.*, vol. 24, no. 2, pp. 919–929, Apr. 2009.

[10] S. Mariéthoz and M. Morari, "Explicit model-predictive control of a PWM inverter with an LCL filter," *IEEE Trans. Ind. Electron.*, vol. 56, no. 2, pp. 389–399, Feb. 2009.

[11] Y. A.-R. I. Mohamed, M. A.-Rahman, and R. Seethapathy, "Robust line-voltage sensorless control and synchronization of LCL-filtered distributed generation inverters for high power quality grid connection," *IEEE Trans. Power Electron.*, vol. 27, no. 1, pp. 87–98, Jan. 2012.

[12] J. Kukkola and M. Hinkkanen, "State observer for grid-voltage sensorless control of a grid-connected converter equipped with an LCL filter," in *Proc. EPE'14-ECCE Europe*, Lappeenranta, Finland, Aug. 2014.

[13] D.-C. Lee and D.-S. Lim, "AC voltage and current sensorless control of three-phase PWM rectifiers," *IEEE Trans. Power Electron.*, vol. 17, no. 6, pp. 883–890, Nov. 2002.

[14] V. Miskovic, V. Blasko, T. M. Jahns, R. D. Lorenz, C. J. Romenesko, and H. Zhang, "Synchronous frame and resonant adaptive observers as disturbance estimators and their applications in power electronics," in *Proc. IEEE ECCE 2014*, Pittsburgh, PA, Sep. 2014, pp. 1248–1255.

[15] J. A. Suul, A. Luna, P. Rodriguez, and T. Undeland, "Voltage-sensor-less synchronization to unbalanced grids by frequency-adaptive virtual flux estimation," *IEEE Trans. Ind. Electron.*, vol. 59, no. 7, pp. 2910–2923, Jul. 2012.

[16] J. A. Suul, A. Luna, P. Rodríguez, and T. Undeland, "Virtual-flux-based voltage-sensor-less power control for unbalanced grid conditions," *IEEE Trans. Power Electron.*, vol. 27, no. 9, pp. 4071–4087, Sep. 2012.

[17] T. Tuovinen, M. Hinkkanen, L. Harnefors, and J. Luomi, "Comparison of a reduced-order observer and a full-order observer for sensorless synchronous motor drives," *IEEE Trans. Ind. Appl.*, vol. 48, no. 6, pp. 1959–1967, Nov. 2012.

[18] J. Kukkola, M. Hinkkanen, and K. Zenger, "Observer-based state-space current controller for a grid converter equipped with an LCL filter: Analytical method for direct discrete-time design," *IEEE Trans. Ind. Appl.*, vol. 51, no. 5, pp. 4079–4090, Sep./Oct. 2015.

[19] J. Kukkola and M. Hinkkanen, "State observer for sensorless control of a grid-connected converter equipped with an LCL filter: Direct discrete-time design," in *Proc. IEEE ECCE 2015*, Montreal, Canada, Sep. 2015, pp. 5511–5518.

[20] R. Teodorescu, M. Liserre, and P. Rodríguez, *Grid Converters for Photovoltaic and Wind Power Systems*. Chichester, United Kingdom: John Wiley & Sons, 2011.

[21] F. D. Freijedo, J. Doval-Gandoy, O. López, and E. Acha, "Tuning of phase-locked loops for power converters under distorted utility conditions," *IEEE Trans. Ind. Appl.*, vol. 45, no. 6, pp. 2039–2047, Nov./Dec. 2009.

[22] C. Blanco, D. Reigosa, F. Briz, and J. M. Guerrero, "Synchronization in highly distorted three-phase grids using selective notch filters," in *IEEE ECCE 2013*, Denver, CO, Sep. 2013, pp. 2641–2648.

[23] C. A. Busada, S. Gómez Jorge, A. E. Leon, and J. A. Solsona, "Current controller based on reduced order generalized integrators for distributed generation systems," *IEEE Trans. Ind. Electron.*, vol. 59, no. 7, pp. 2898–2909, Jul. 2012.

[24] M. Liserre, R. Teodorescu, and F. Blaabjerg, "Multiple harmonics control for three-phase grid converter systems with the use of PI-RES current controller in a rotating frame," *IEEE Trans. Power Electron.*, vol. 21, no. 3, pp. 836–841, May 2006.

[25] M. H. J. Bollen, "Characterisation of voltage sags experienced by three-phase adjustable-speed drives," *IEEE Trans. Power Del.*, vol. 12, no. 4, pp. 1666–1671, Oct. 1997.

Jarno Kukkola received the B.Sc. (Tech.) and M.Sc. (Tech.) degrees from Aalto University, Espoo, Finland, in 2010 and 2012, respectively, where he is currently working toward the D.Sc. (Tech.) degree in the School of Electrical Engineering. His research interests include grid-connected converters.

Marko Hinkkanen (M'06–SM'13) received the M.Sc.(Eng.) and D.Sc.(Tech.) degrees from Helsinki University of Technology, Espoo, Finland, in 2000 and 2004, respectively.

Since 2000, he has been with Helsinki University of Technology (part of Aalto University, Espoo, since 2010). He is currently an Assistant Professor with the School of Electrical Engineering, Aalto University. His research interests include power-electronic converters, electric machines, and electric drives.